

Chemical Science

Accepted Manuscript

This article can be cited before page numbers have been issued, to do this please use: M. Bose, M. Kangsabanik, D. Dey, R. N. Gayen, M. K. Panda and P. Naumov, *Chem. Sci.*, 2026, DOI: 10.1039/D6SC01505K.



This is an Accepted Manuscript, which has been through the Royal Society of Chemistry peer review process and has been accepted for publication.

Accepted Manuscripts are published online shortly after acceptance, before technical editing, formatting and proof reading. Using this free service, authors can make their results available to the community, in citable form, before we publish the edited article. We will replace this Accepted Manuscript with the edited and formatted Advance Article as soon as it is available.

You can find more information about Accepted Manuscripts in the [Information for Authors](#).

Please note that technical editing may introduce minor changes to the text and/or graphics, which may alter content. The journal's standard [Terms & Conditions](#) and the [Ethical guidelines](#) still apply. In no event shall the Royal Society of Chemistry be held responsible for any errors or omissions in this Accepted Manuscript or any consequences arising from the use of any information it contains.

ARTICLE

Tunable Synaptic Memory Response Using Organic Regioisomeric Donor-Acceptor-Donor Luminophore Triads

Mainak Bose,^{a†} Manoj Kangsabanik,^{b†} Dibyendu Dey,^{a†} Panče Naumov,^{c,d,e,f*} Rabindra Nath Gayen^{b*}, Manas K. Panda^{a*}Received 00th January 20xx,
Accepted 00th January 20xx

DOI: 10.1039/x0xx00000x

Abstract: Modeling synaptic memory with small molecular compounds allows for replication of key features of biological learning and memory in a simplified, controllable, and tunable chemical system, where processes such as signal transmission, plasticity, and information storage can be realized without the complexity of the full biological networks. Aimed at probing the substitution effects on the molecular conjugation and optoelectronic and neuromorphic performance, here we report novel regioisomeric donor-acceptor-donor (DAD) fluorophores that are utilized for optoelectronic synaptic memory devices. The photophysical characterization revealed substitution-dependent solid-state luminescence across the visible spectrum and variation in lifetimes that are attributed to the combination of molecular packing and charge-transfer characteristics. Diffraction methods and theoretical calculations elucidated the structure–property relationships, highlighting the effect of regiochemistry on the π – π interactions and molecular orbitals. The materials display synaptic memory responses in two-terminal organic devices, demonstrating key neuromorphic functionalities such as paired-pulse facilitation and long-term potentiation. This study introduces design guidelines for multifunctional organic semiconductors by regioisomerism, with potentials for applications that extend to solid-state lighting, sensing, memory devices, and bioinspired computing.

Introduction

In the age of artificial intelligence, rapid advancements are being pursued in the fields of data perception for human-machine interfaces, robotics, and prosthetic technologies. The human visual system is an impressive biological tool capable of both perception and processing of photo stimuli (input data) via a variety of synaptic plasticity rules—including both volatile and non-volatile components—to channelize various information to the brain. Within the human visual system, the synaptic plasticity describes the brain's capacity to acclimate and reorganize its neural connections, especially at synaptic level, in response to sensory information. This adaptability enables perceptual learning, visual change, and adaptation to variations of intensity and colour of light. Replicating such

functionalities of the natural visual system by artificial synaptic devices is known to pose significant challenges with photoresponsive efficiency, integration of distinct components, compatibility, energy consumption, and processability.^{1–3} Various inorganic materials, including metal oxides, 2D materials, and perovskites, have been employed in artificial optoelectronic devices to emulate the synaptic memory behaviour, with notable success documented recently.^{4–15} Conversely, organic crystalline materials have only recently garnered attention as flexible optoelectronic and memory components, primarily due to the ease of their synthesis, relatively lower toxicity, affordability, solution-based processability at ambient conditions, and the unrivalled opportunities they provide for tuning of their properties through molecular design.^{16–31} The intrinsic advantages brought about by electron delocalization and defect-induced charge trapping favour donor-acceptor charge-transfer conjugated molecules with planar or rigid structures as materials for organic field-effect transistors and memory devices.³² These organic materials act as photo-absorbers in three-terminal devices where photoexcitation, under external electric potential from the gate electrode, mimics the presynaptic event, and subsequent response current between the source and drain electrodes is analogous to the post synaptic event. Such artificial organic architectures essentially replicate the cognitive operation of biological synaptic organs, exemplified by paired pulse facilitation (PPF), long- and short-term plasticity (LTP and STP), excitatory postsynaptic current (EPSC), spike-number-dependent plasticity (SNDP), and conversion from volatile to non-volatile memory states.^{10,12,14} Various mechanisms of photosynaptic functions, including charge carrier trapping,^{9,19}

^a Department of Chemistry, Jadavpur University, Kolkata-700032, India. E-mail: manaspanda.chemistry@jadavpuruniversity.in

^b Department of Physics, Jadavpur University, Kolkata-700032, India. E-mail: rgayen.physics@jadavpuruniversity.in

^c Smart Materials Lab, Division of Science and Mathematics and Smart Materials Lab, New York University Abu Dhabi, 129188 Abu Dhabi, UAE

^d Center for Smart Engineering Materials, New York University Abu Dhabi, 129188 Abu Dhabi, UAE

^e Research Center for Environment and Materials, Macedonian Academy of Sciences and Arts, MK-1000 Skopje, Macedonia

^f Molecular Design Institute, Department of Chemistry, New York University, New York, New York 10003, United States. E-mail: pance.naumov@nyu.edu

[†]These authors contributed equally in this work.

* Footnotes relating to the title and/or authors should appear here.

Supplementary Information available: [details of any supplementary information available should be included here]. See DOI: 10.1039/x0xx00000x



photoactive electrets, and oxygen-induced defects,^{1,2,7,18} have been proposed. Despite notable progress, the development of multifunctional organic molecules that can withstand the challenges of facile synthesis, structural and property tunability, alongside superior capabilities as synaptic memory devices, remain elusive.

Herein, we report a series of donor-acceptor-donor (DAD) type regioisomeric luminescent organic triads that function conceptually equivalent to light-responsive synaptic memory elements, with the device behaviour being determined by isomerism (Figure 1a, b). These DAD molecules exhibit a criss-cross type 3D molecular arrangement featuring void channels that facilitates charge carrier transport and trapping necessary for synaptic memory function. The molecules, prepared in single step, contain cyanostilbene acceptor

(A) core with two terminals containing -OMe donor (D) groups in various dispositions (Figure 1b). The regioisomeric variation in the donor on the phenyl ring was found to impact strongly both the fluorescence properties and the photosynaptic memory response with various pulses and very high photoconductivity. This approach introduces a new dimension to materials design for neuromorphic electronics, where synergistic application of light and molecular design is used to control artificial synaptic functions. To our knowledge, this report is the first demonstration where regioisomerism alone can tune synaptic memory responses in optoelectronic devices, thereby combining molecular chemistry with advanced neuromorphic functionality.

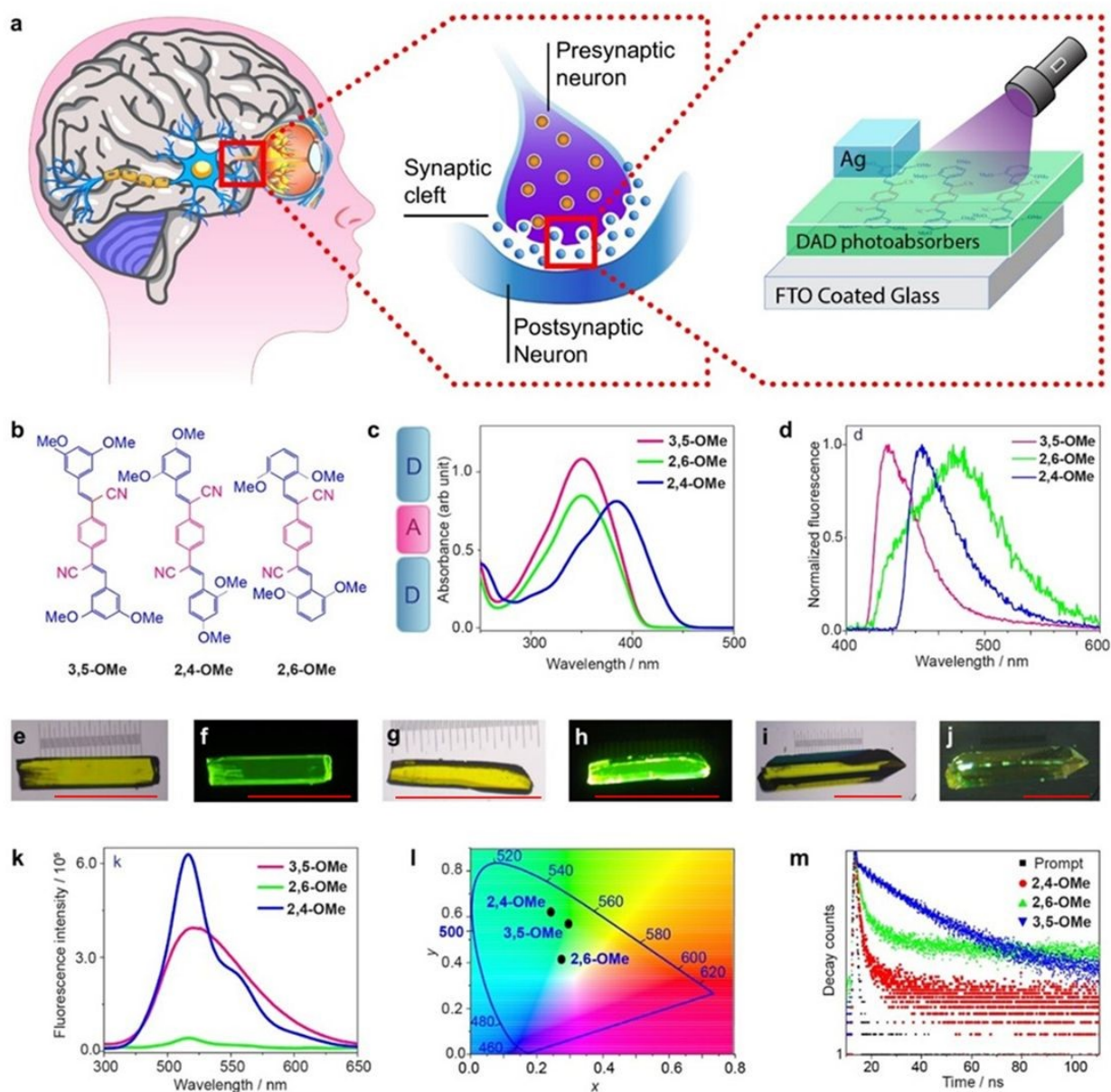


Figure 1. a) Model representation of the function of synaptic memory organ and artificial device. (b) Chemical structures of the donor-acceptor-donor (DAD) type isomers. The DAD components in the structures and the sketch are highlighted in different colors. (c, d)



Absorbance (c) and normalized fluorescence (d) spectra recorded in a chloroform solution. (e-j) Microscopic images of the crystals with 1 mm scale bar in red colour: (e) **3,5-OMe** crystal in ambient light and (f) under UV light, (g) **2,4-OMe** crystal in ambient light, and (h) under UV light, (i) **2,6-OMe** crystal in ambient light and (j) under UV light. (k) Solid-state fluorescence spectra of the DAD isomers. (l) Emission of the isomers on a CIE-1931 plot x, y coordinates: **3,5-OMe** (0.294, 0.569); **2,4-OMe** (0.244, 0.619); **2,6-OMe** (0.274, 0.415). (m) Fluorescence decay curves of the three isomers

Result and Discussion

The compounds were synthesized by a one-step Knoevenagel condensation between *p*-xylylene dicyanide and the respective aldehydes in moderate to good yields (ESI Scheme S1) and characterized using standard methods (Figures S1-S10, ESI). As Figure 1b depicts, the isomers differ from each other by the -OMe substitution on the terminal phenyl rings, while they share the common central acceptor moiety, and all are extensively conjugated. The UV-Vis spectra (chloroform, 1×10^{-5} M) of **3,5-OMe** and **2,6-OMe** contain peaks from the π - π^* transition with maximum absorption $\lambda_{\max} = 351$ nm and 349 nm for the two compounds, respectively. The absorption of **2,4-OMe** is red-shifted relative to the other two isomers, to 384 nm, due to the combined electronic contribution of the ortho- and para-substitution that effectively decreases the HOMO-LUMO gap. On the contrary, the steric crowding at two ortho-positions in the **2,6-OMe** isomer leads to a non-planar, twisted structure, and gives rise to high-energy absorption maxima.

All the isomeric compounds are poorly emissive in solution (Figure 1d). However, unlike **2,6-OMe**, the two other compounds are strongly emissive in the solid state. As observed from Figure 1k, the spectrum of the crystal of **2,4-OMe** contains two emission bands with $\lambda_{\max} = 516$ nm and a shoulder at 556 nm (CIE coordinates: 0.244, 0.619; Figure 1l). **3,5-OMe** exhibits broad, structureless emission around 521 nm (CIE coordinates: 0.294, 0.569). The decay of the fluorescence of **2,4-OMe** is biexponential, with lifetime of 2.445 ns (50.88%) and 16.498 ns (49.12%), while that of **3,5-OMe** was fitted with a single-exponential function that afforded a lifetime of 17.445 ns (Figure 1m, ESI Table S1). In contrast to these isomers, **2,6-OMe** is poorly emissive in both solid state and in solution (Figure 1i-k), and shows a weak emission at $\lambda_{\max} = 516$ nm (CIE coordinates: 0.274, 0.415). This is likely due to the presence of two ortho-dispositioned bulky -OMe groups which causes the molecule to be twisted, and disrupts the conjugation between the donor and the acceptor.

Density functional theory (DFT) calculations support the above conclusion, indicating smallest HOMO-LUMO gap for **2,4-OMe** (3.21 eV) and highest for **2,6-OMe** (3.50 eV), with **3,5-OMe** having an intermediate value (3.41 eV). The experimental band gaps were calculated from the respective solid state absorption spectra using Tauc plot corroborate with the above trend (Figure S11, ESI). The LUMOs are spread mostly across the central core of all molecules, while the HOMOs reside mostly on the terminal phenyl rings containing -OMe groups (Figure 2). These variations in emission reflect its "tunability" by means of altering the position of the donor

functional groups. Excited-state calculations, performed by using the TDDFT method to examine the transitions responsible for the emission, identified the π - π^* transition at 438.8 nm from level HOMO-1 to LUMO+1 with excitation energy of 2.83 eV and oscillator strength of 1.94 as the major contributor to the emission in **2,4-OMe**. In case of **3,5-OMe**, the 344.9 nm band was calculated as π - π^* transition at 3.60 eV with oscillator strength of 1.74 and occurs between levels HOMO to LUMO. In contrast with the other two isomers, however, for **2,6-OMe** the gap of 4.09 eV and oscillator strength of 0.11 arise due to a π - π^* transition from energy level HOMO-2 to LUMO corresponding to the wavelength 303.2 nm. The lower strength of the oscillator corresponding to the transition in **2,6-OMe** isomer is in accord with its weak emission, and can be traced back to its twisted molecular conformation (see below).

The observed significant substituent effects on the solid-state luminescence and other optoelectronic properties were rationalized by the crystal structures of all isomers (Figure 3, ESI Table S2). The experimental powder X-ray diffraction patterns of the samples matched well their simulated (from the crystal structure) counterparts, and confirmed the phase purity of all compounds (Figures S12-S14, ESI). As shown in Figure 3, while the molecular conformations of **3,5-OMe** and **2,4-OMe** are nearly planar, that of **2,6-OMe** is twisted. In **3,5-OMe** and **2,4-OMe**, the terminal phenyl rings are nearly coplanar with the central phenyl ring (interplanar angles: $\sim 4.7^\circ$ and $\sim 2.9^\circ$, respectively, Figure 3a, b, Figures S15, ESI), suggesting strong electronic communication within the DAD skeleton. Both **3,5-OMe** and **2,4-OMe** adopt a slip-stacked *J*-type aggregation with slip angles $\sim 48^\circ$ and 27° , respectively (Figure 3d, e, Figure S16, ESI). The small slip-angles in **3,5-OMe** and **2,4-OMe** facilitate stacking between the layers, enhance the donor-acceptor charge-transfer interaction, and result in red-shift in the emission (Figure 1k). In contrast to the other two isomers, as is clearly observed from the overlapped molecular representation in Figure 3g, the molecule of **2,6-OMe** is twisted due to steric crowding of the -OMe groups, with an angle of $\sim 69.5^\circ$ between its terminal and central benzene rings (Figure 3c). This molecular distortion, as pointed out above, accounts for quenching of the fluorescence in the solid state



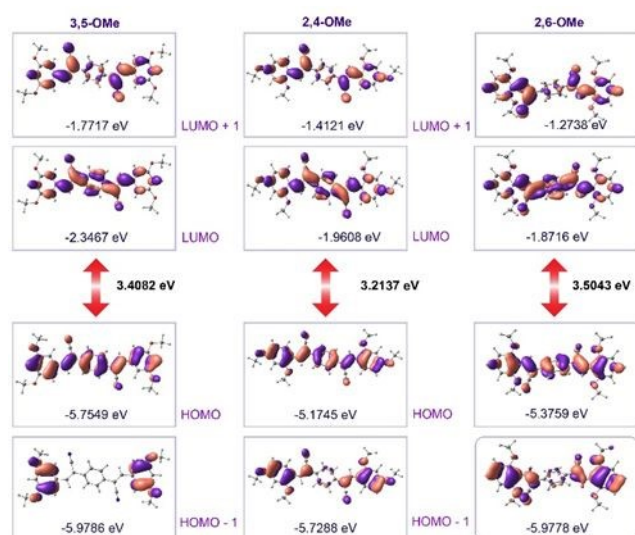
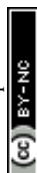


Figure 2. DFT (B3LYP/6-31G*) computed electron isosurfaces of the frontier molecular orbitals of isomeric compounds.

Crystallographic face indexing, simulated crystal habits, and analysis of the molecular packing are provided in the Figures S17–S20, ESI† in the structure of **3,5-OMe**, hydrogen bonds between the nitrile group and aromatic protons of the central ring ($C3-H3A \cdots N1$, $d(C3 \cdots N1) = 3.4 \text{ \AA}$, $\angle(C3-H3A \cdots N1) = 143.4^\circ$) connect the neighbouring molecules and extend roughly along the crystallographic *c*-axis (Figure 3h, i). $O \cdots H$ interactions involving methoxy oxygen and methyl protons ($C8-H8A \cdots O2$, $d(C8 \cdots O2) = 3.5 \text{ \AA}$, $\angle(C8-H8A \cdots O2) = 163^\circ$; $C7-H7C \cdots O2$, $d(C7 \cdots O2) = 3.5 \text{ \AA}$, $\angle(C7-H7C \cdots O2) = 157.2^\circ$) are also present in the crystal lattice. The planar and rigid conformation allows for *J*-type aggregation with opportunity for intramolecular exciton coupling and results in the strong fluorescence (Figure S16, ESI). The molecules in the crystal of **2,4-OMe** adopt a more planar (interplanar angle, 3.0°) and rigid geometry, supported by hydrogen bonding involving the methoxy oxygen atom and neighbouring methoxy hydrogen atoms ($C2-H2A \cdots O1$, $d(C2 \cdots O1) = 3.4 \text{ \AA}$, $\angle(C2-H2A \cdots O1) = 136.8^\circ$, Figure 3j, k) and a weak, non-classical interaction ($C14-H14 \cdots C2$, $d(C14 \cdots C2) = 3.5 \text{ \AA}$, $\angle(C14-H14 \cdots C2) = 124.3^\circ$, Figure 3j, k). In the case of **2,6-OMe**, the sterically twisted molecules in the lattice are arranged in an antiperiplanar fashion. Except for a weak hydrogen bond ($C13-H1 \cdots C1$, $d(C13 \cdots C1) = 3.7 \text{ \AA}$, $\angle(C13-H13 \cdots C1) = 149.7^\circ$, Figure 3l), no other intermolecular interactions were observed.



ARTICLE

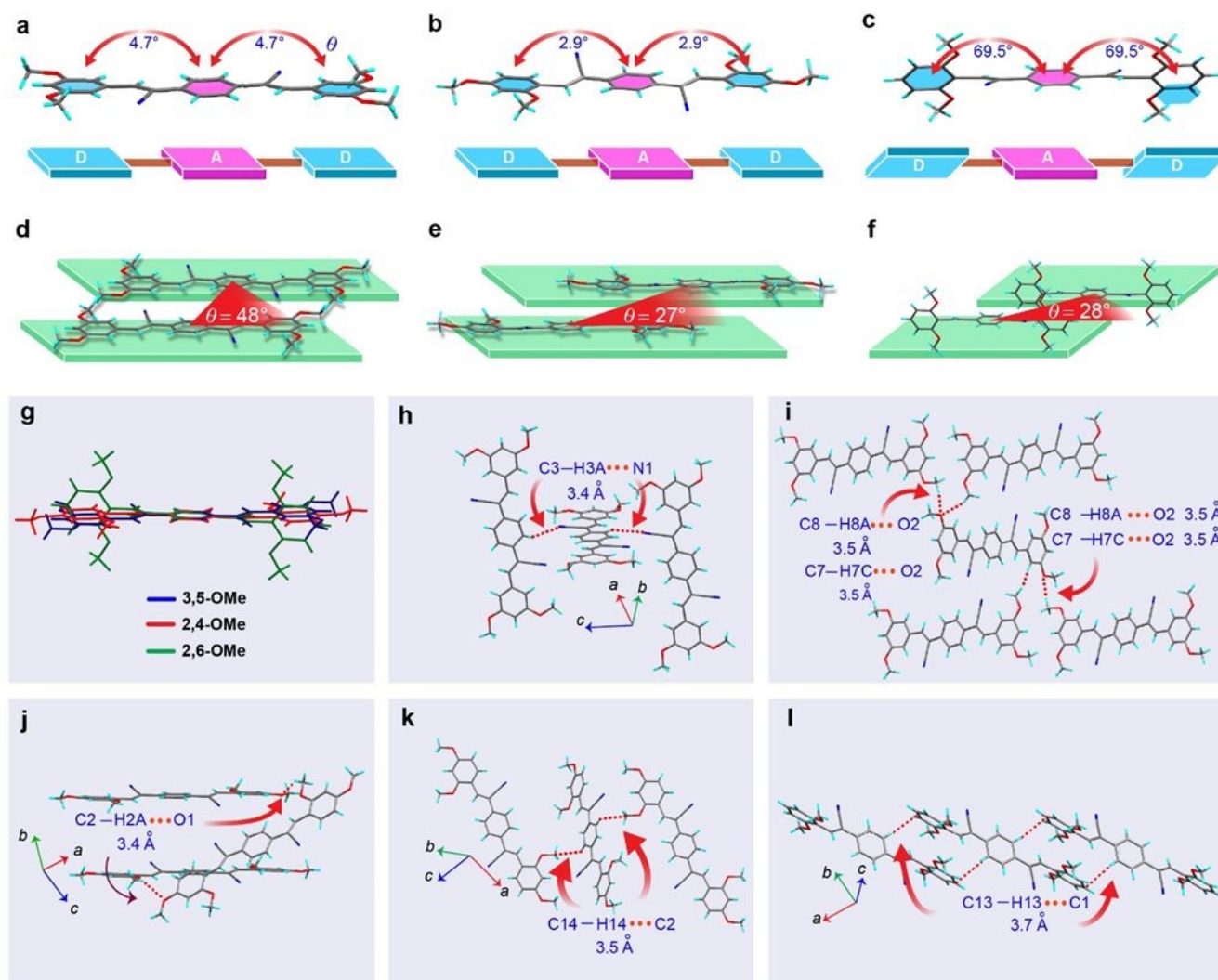


Figure 3. (a-c) Molecular conformations in the crystals of **3,5-OMe** (a), **2,4-OMe** (b), and **2,6-OMe** (c). (d-f) Slip-stacked disposition and associated angles in the structures of **3,5-OMe**, **2,4-OMe**, and **2,6-OMe**. (g) Overlaid representation of the experimentally determined conformations of the three isomers. (h-l) Intermolecular interactions in the crystal lattices of **3,5-OMe** (h, i), **2,4-OMe** (j, k), and **2,6-OMe** (l).

Considering that pores and voids in the crystal lattice usually play important roles in charge transport and related optoelectronic performance, we analysed the empty space in the three crystals (Figure S21, ESI). The crystal lattice of **2,4-OMe** contains 24.4% void space, while those of **3,5-OMe** and **2,6-OMe** have 20.05% and 19.2% respectively, relative to the respective unit cell volumes. These pores could act as potential trap for the charges and affect conductivity (see below). While the initial charge injection is driven by the applied electric field and quantum mechanical tunnelling, the effective

capture and immobilization of the carrier at an attractive trap site (void space) are strongly reinforced by intermolecular interactions, coulombic attraction, and dispersive energy. Hirshfield surface analysis and the related energy framework calculation (Figures S22-S27, and Tables S3-S9, ESI) revealed that **3,5-OMe** and **2,4-OMe** isomers possess higher Coulombic interaction energy relative to **2,6-OMe**, which accounts for their better optoelectronic synaptic memory performance (discussed below). Furthermore, non-covalent H...H, C...H, O...H, and N...H interactions present in the structures of

2,4-OMe and **3,5-OMe** are expected to play pivotal role in lattice stabilization for charge trapping and mobilization that is crucial for optimal device performance and reliability.

The dependence of the fluorescence of these structurally isomeric DAD materials prompted us to explore their potential for optoelectronic synaptic memory applications. To that end, thin film devices were spun-coated on FTO glass (Figure 1a). The surface morphology of solution-processable thin films (drop-casted on silicon wafer for inspection) were investigated by scanning electron microscopy (SEM). As shown in Figure 4a-f, the films display distinct crystalline morphology with variable size and shape of the crystallites for different isomers—an important parameter governing the synaptic memory response in the respective devices. The thickness of the films was measured by SEM analysis (Figure S28, ESI) and the crystallinity of the films was confirmed by X-ray diffraction analysis (Figure S29, ESI). Each device (Figure 1a) was illuminated with five consecutive UV pulses (365 nm, 8 $\mu\text{W}/\text{cm}^2$) under an external bias of +100 mV, during 25 s on/off intervals (Figure S30, ESI). The figures of merit for the photodetection performance of the devices³³ are summarized in Table 1. Each device exhibited excellent photoresponsivity (R) and specific detectivity (D^*). Among the three isomers, the device prepared from **3,5-OMe** were found to have optimal performance, with outstanding photoresponsivity of 41.25 A/W and specific detectivity of 4.57×10^{11} Jones.

Table 1. Performance metrics of the devices under 365 nm wavelength (8 $\mu\text{W}/\text{cm}^2$) at +100 mV bias:

Material	Photocurrent / μA	Responsivity / (A/W)	Detectivity / 10^{11} Jones
2,4-OMe	13	16.25	2.12
3,5-OMe	33	41.25	4.57
2,6-OMe	10	12.50	2.10

In the devices based on **2,4-OMe**, the strong intramolecular electronic communication facilitated by favourable donor-acceptor stacking allows a large number of electrons to be photoexcited from the HOMO to the LUMO upon UV illumination. However, the low excited-state lifetime of **2,4-OMe** causes these electrons to rapidly de-excite back to the HOMO before the applied bias can effectively drive them, and therefore result in low photocurrent. The higher photo-current in the **3,5-OMe**-based devices is attributed to their longer excited-state lifetime, planar molecular structures with enhanced conjugation, and higher coulombic and dispersive energies. The longer lifetime and higher dispersive energy allow photoexcited electrons to be driven by the bias, resulting in stronger current. Conversely, the twisted structure of **2,6-OMe** reduces conjugation and lowers lattice dispersive energy, leading to fewer electrons being excited to the LUMO upon UV illumination. Despite having a longer excited carrier lifetime, the limited number of photoexcited carriers results in the lowest photocurrent among the three device types.

In the photoresponse I-t curves, all devices demonstrated intriguing behaviour: after the UV light was turned off, the devices did not return to their initial states, but instead the effect of the excitation was sustained (Figure 4g-i). This observation clearly indicates the potential of the materials for artificial synaptic visual memory applications. Synapses act as bridges for communication of electrical signals between presynaptic and postsynaptic neurons, as schematically depicted in Figure 1a. External light stimuli, i.e., visual information, are processed by the retina through interconnected neurons and synapses.²¹ Given the capabilities of the molecules **2,4-OMe**, **3,5-OMe**, and **2,6-OMe** for “memorizing” visual information, we carried out systematic investigations at an external bias of +100 mV using sequential UV-light pulses (equivalent to presynaptic stimuli) with various intervals and different numbers of pulses. The experiments were carried out by applying five sequential pulses (365 nm, 8 $\mu\text{W}/\text{cm}^2$) to the devices with a pulse width (T) of 10 s and an interval (Δt) of 2 s. The results, shown in Figure 4g-i, evidence significant increase in current under UV illumination, which is attributed to the excitatory postsynaptic current (ΔEPSC). For all devices, the second light pulse (A_2) significantly enhanced the ΔEPSC compared to the initial pulse (A_1). This elevation in postsynaptic response relative to a subsequent presynaptic input established the paired-pulse facilitation (PPF) characteristics of the organic molecules. The PPF behaviour is likely due to the inability of the photogenerated charge carriers to return to their primary state before the arrival of the next pulse; as a result, the newly generated carriers accumulate along with the previously gathered ones, thereby significantly enhancing the ΔEPSC compared to the ΔEPSC induced by the first pulse.²¹ After application of five consecutive pulses, the devices were further monitored for another minute (60 s) to test their “memory retention” (Figure 4g-i). This experiment revealed that **2,4-OMe** could hold the effect of UV-induced external stimuli without a significant loss. Based on these initial investigations, the excellent retention capability of **2,4-OMe** makes it particularly suitable for artificial synapse applications.

The presynaptic plasticity, which is a measure of the dependence of synaptic response strength on the timing and pattern of the synaptic inputs, can be evaluated through paired-pulse facilitation (PPF) and post-tetanic potentiation (PTP) index, which are defined in Eqs. 1 and 2:

$$\text{PPF} = \frac{A_2}{A_1} \times 100\% \quad (1)$$

$$\text{PTP} = \frac{A_5}{A_1} \times 100\% \quad (2)$$

where A_1 , A_2 , and A_5 represent the post-synaptic current corresponding to the first, the second, and the fifth pulse, respectively. To study the decay dynamics of the artificial synapses, all the devices were investigated under UV pulses ($t = 10$ s) with different intervals ($\Delta t = 2, 5, 10, 15, 20$, and 25 s). The variations of the PPF and PTP indices are shown in Figure 4j-l. With the increase in the pulse intervals, both the PPF and PTP indices initially fall drastically, before near saturation for higher time intervals. Both the



PPF and PTP indices were fitted using double-exponential decay functions modelled with Eq 3:²¹

$$\text{PPF (or PTP)} = C_0 + C_1 \exp\left(-\frac{\Delta t}{\tau_1}\right) + C_2 \exp\left(-\frac{\Delta t}{\tau_2}\right) \quad (3)$$

where the two different time constants τ_1 and τ_2 are attributed to the characteristic relaxation times corresponding to the rapid and slow decay phases of the synapse, respectively. The extracted values of τ_1 and τ_2 corresponding to the PPF and PTP indices of all the devices are available from the insets of Figures 4j-l. For the **2,4-OMe**-based devices, the relaxation times were determined to be 0.099 s / 109243.72 s and 0.98 s / 5.39 s, corresponding to the PPF and PTP,

respectively. The much lower value of τ_1 as compared to τ_2 is very similar to the decay dynamics observed in biological synapses. The **2,6-OMe**-based devices had also shown a similar tendency with relaxation times of 0.24 s / 6.03 s and 0.14 s / 9471.92 s corresponding to the PPF and PTP, respectively. However, for the **3,5-OMe**-based devices, although the decrease of the PTP index with interval time mimicked the biological synapses well (0.159 s / 2845.2 s), the PPF index showed a decay that was close to exponential (5.43 s / 5.43 s). The very fast "rapid decay phases" ($\tau_1 = 0.099$ s) and much slower "slow decay phases" ($\tau_2 = 109243.7$ s) favor **2,4-OMe** as the best candidate for artificial synaptic memory applications among the DAD isomers.

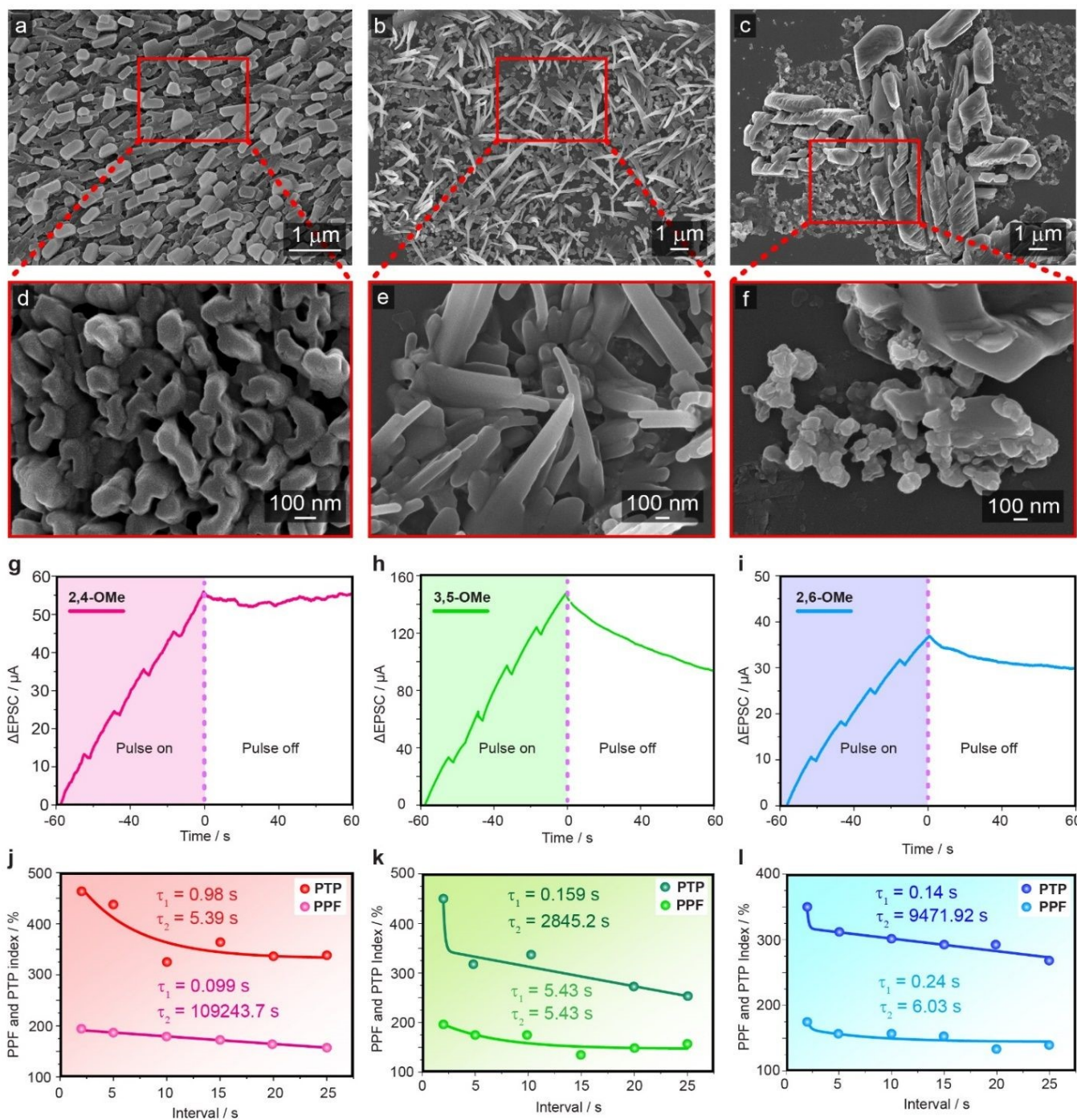


Figure 4. (a-f) SEM image of drop-cast samples of **3,5-OMe** (a,d), **2,6-OMe** (b,e), and **2,4-OMe** (c,f). (g-i) Changes in EPSC in response to 365 nm pulses, featuring a width of 10 s and 2 s interval at +100 mV bias of **2,4-OMe** (g), **3,5-OMe** (h), **2,6-OMe** (i) synaptic memory devices. (j-l) Variation of PPF and PTP indices with pulse intervals of synaptic memory devices based on **2,4-OMe** (j), **3,5-OMe** (k), and **2,6-OMe** (l).

The number of incident UV pulses can affect the plasticity of the artificial synaptic memories. To study these effects, namely spike-number-dependent plasticity (SNDP), the devices were illuminated with different numbers (2, 5, 10, and 15) of UV-pulses ($T = \Delta t = 10$ s), as shown in Figure 5a-c, aimed at identifying their synaptic nature and memory retention capability. For the **2,4-OMe**-based devices, the EPSC increases almost linearly with increasing number of pulses (Figure 5a). However, in case of the **3,5-OMe** and **2,6-OMe**-based devices, the EPSC tends to saturate with increased number of pulses

(Figure 5b, c). The EPSC corresponding to the first pulse (A_1) and the n^{th} pulse (A_n ; $n = 2, 5, 10$, and 15) are depicted in the comparative bar diagrams in Figure 5d-f. All devices were further observed for another 60 s to verify the effect of the UV-pulses on their plasticity. With increasing number of pulses, the **2,4-OMe**-based devices are able to uphold their long-term plasticity (LTP), whereas in case of the other two devices the EPSCs decreases during post-initiation.

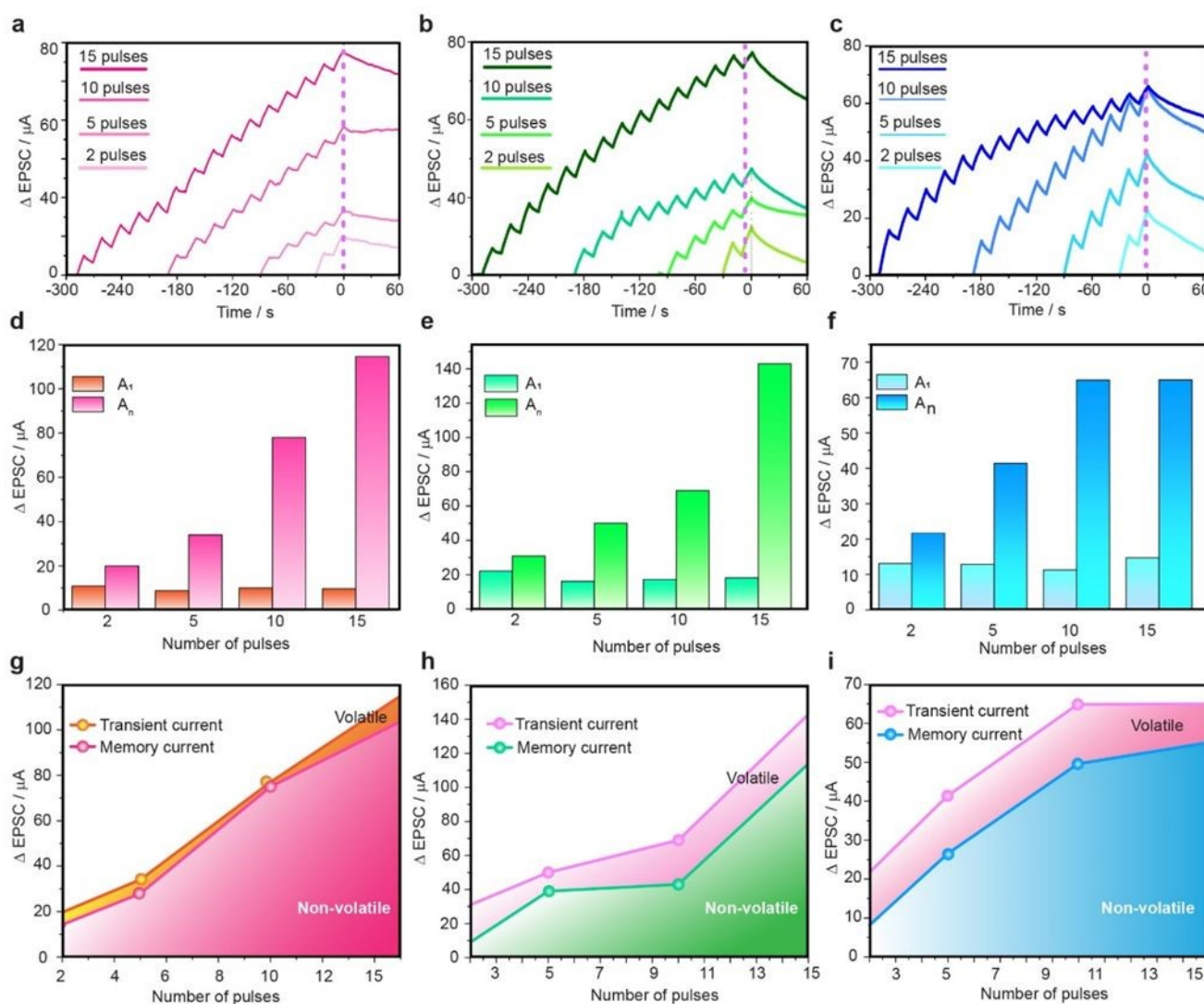


Figure 5. (a-c) Variations in EPSC in response to different no of 365 nm pulses (width of 10 s and interval of 10 s) at +100 mV bias for memory devices based on **2,4-OMe** (a), **3,5-OMe** (b), and **2,6-OMe** (c). (d-f) The EPSC spike of A_1 and A_n of synaptic memory devices based on **2,4-**



OMe (d), **3,5-OMe** (e) and **2,6-OMe** (f). (g-i) Variations of transient current and memory current with different number of pulses of synaptic memory devices based on **2,4-OMe** (g), **3,5-OMe** (h), and **2,6-OMe** (i).

DOI: 10.1039/D6SC01505K

The variation of transient current (current spiked relative to the initial current after n UV-pulses) and the memory current (the change in current relative to the initial current 60 seconds after switching off the pulses) with the number of pulses are depicted in Figure 5g-i. Figure 5g shows that **2,4-OMe**-based devices have very small volatility; they can retain the visual information even after a large number of pulses, which translates into large amount of data. Although **3,5-OMe**- and **2,6-OMe**-based devices also exhibit very

good memory retention, their performance is not as efficient relative to **2,4-OMe**. The SNDP gain values (A_n/A_1) show a linear trend with the pulse numbers for **2,4-OMe**-based devices (Figure S31, ESI). The **3,5-OMe**-based devices show a non-linear increasing SNDP gain with the number of pulses, however the SNDP gain of the **2,6-OMe**-based devices is decreasing (Figure S31, ESI).

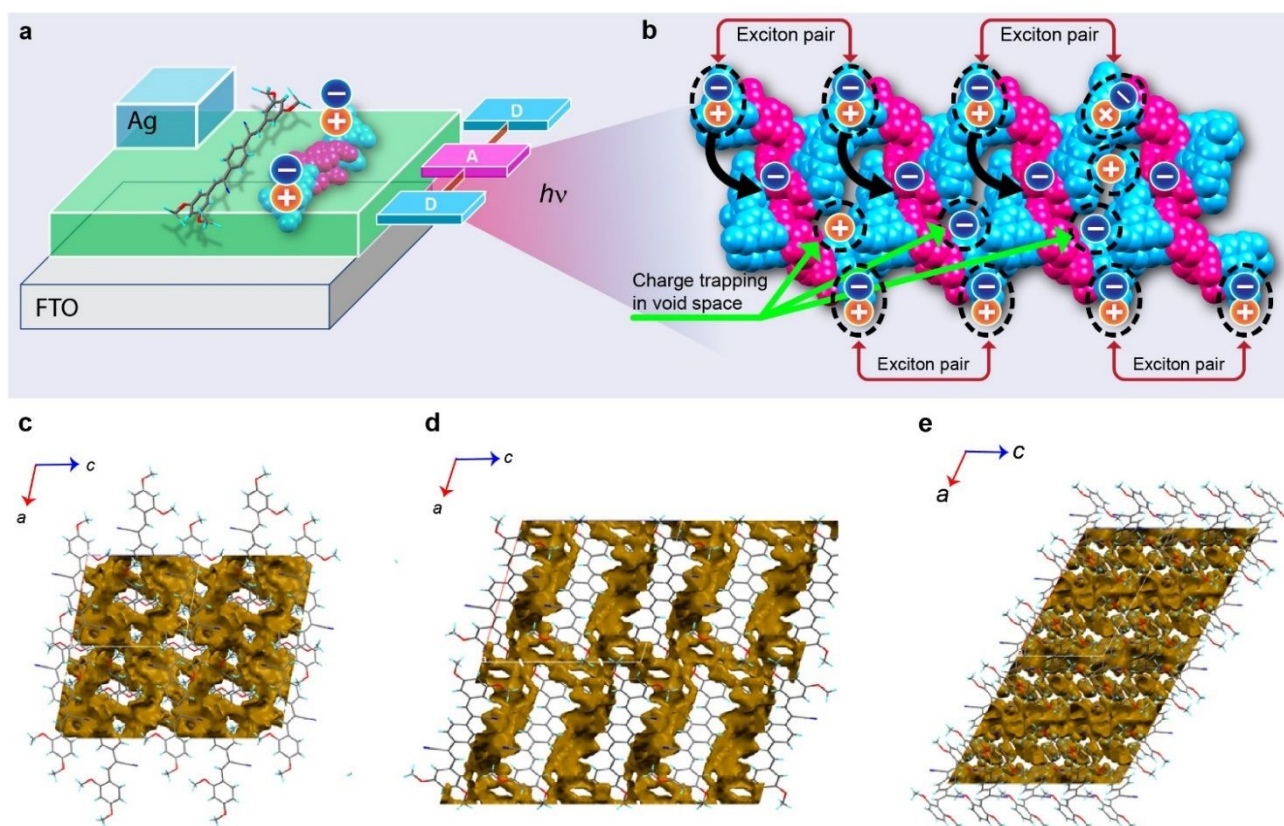


Figure 6. (a, b) Possible mechanistic model of the photosynaptic behaviour in DAD isomers. (c-e) Pore analysis of **2,4-OMe** (c), **3,5-OMe** (d), and **2,6-OMe** (e)

Persistent photoconductivity (PPC) in crystalline DAD molecules is a complex phenomenon driven by several key factors. The primary mechanisms are trap-assisted charge storage, defect-mediated transport, and structural effects. The intrinsic pores and structural imperfections within the crystalline DAD frameworks, such as vacancies and disordered packing, create high density of localized mid-gap states. These states act as charge traps, capturing photogenerated electrons or holes, as depicted schematically in Figure 6a, b. The trapping delays the recombination of charge

carriers, which are then released slowly after the cessation of light excitation, thereby sustaining conductivity. Additionally, the strong intramolecular charge transfer character brought about by the DAD structure plays a crucial role. Upon light absorption, electrons are promoted from the donor to the acceptor units, creating spatially separated electron-hole pairs that hinders their recombination, thereby prolonging carrier lifetimes and contributing to the persistent conductivity. The retention characteristics of the devices were investigated by illuminating the samples under UV light for 300 s (UV-ON), followed by a 1200 s dark period (UV-OFF). Notably, after



1200 s in the dark, the **2,4-OMe** and **3,5-OMe** devices retain a high fraction of their photocurrent (~62% and ~60%, respectively).³⁶⁻³⁸ In contrast, the **2,6-OMe** device exhibits significantly poorer retention (~21%) (Figure S32, ESI), indicating inferior charge storage or trapping stability. The analysis of the void space and energy framework calculation in the structures of the three isomers in Figure 6c-e reveals distinct differences. The 2,4-isomer exhibits the largest void space at 24.4%, followed by the 3,5-isomer at 20%, and the 2,6-isomer at 19%. Moreover, higher lattice Coulombic interaction energy in the 2,4-isomer facilitates stronger charge binding. The superior synaptic memory performance of **2,4-OMe** is a result of a combination of these factors. The highest percentage of voids in its crystalline structure provides large number of charge traps. In conjunction with the high degree of intermolecular charge transfer due to the small slip-angle, this asset favours this material for optoelectronic synaptic memory applications, as described above. In contrast, **2,6-OMe** has the least available void space, smaller Coulombic interaction energy and highly twisted structure, which significantly reduces the conjugation and hinders intramolecular charge transfer, resulting in the weakest PPC performance out of the three materials. To gain deeper insight into the trapping/de-trapping dynamics responsible for the persistent photocurrent (PPC) behavior, the time-dependent current response in both the growth (UV-ON) and decay (UV-OFF) regimes was analysed using a bi-exponential fitting function (Eq. 4). Such a response is widely regarded as a hallmark of heterogeneous trap distributions and multi-scale charge relaxation processes.³⁵

$$I = I_0 + A_f e^{-\frac{t}{\tau_f}} + A_s e^{-\frac{t}{\tau_s}} \quad (4)$$

Here, τ_f and τ_s represent the fast and slow response time constants, respectively, while A_f and A_s are the corresponding pre-exponential coefficients. The underlying mechanism of the persistent photocurrent (PPC) behavior is schematically illustrated in Figure S33, ESI. During the rising phase (UV-ON), the fast component is attributed to the prompt photoexcitation of charge carriers from the HOMO to the LUMO, whereas the slow component originates from the gradual filling of trap states. In contrast, during the decay phase (UV-OFF), the fast time constant corresponds to the rapid recombination of free carriers, while the slow component is associated with the delayed release (de-trapping) of carriers from trap states. Notably, deep trap states, located further within the bandgap, require higher thermal activation energy for carrier release, resulting in a significantly prolonged decay process and slower recovery of the dark current.³⁹⁻⁴³ The extracted fitting parameters for all three samples are summarized in the table S10, ESI. The fitting parameters presented in the table indicate that, during the rising phase, the photoresponse of the **2,4-OMe** and **3,5-OMe** devices is predominantly governed by the trap-filling process, suggesting a substantial population of charge carriers being captured by both shallow and deep trap states. In contrast, the **2,6-OMe** device exhibits a response primarily dominated by direct photo-generation, corresponding to charge carrier transitions from the HOMO to the LUMO. Owing to its relatively inferior molecular conjugation, the **2,6-OMe** sample displays a comparatively larger time constant associated with the photo-generation process. Furthermore, the minimal contribution of the trap-filling component during the rising phase indicates a significantly reduced density of

accessible trap states, leading to negligible charge trapping during photoexcitation in the **2,6-OMe** device. During the falling phase, the decay dynamics for all devices are predominantly governed by thermally activated de-trapping of charge carriers from both deep and near band-edge trap states. Although the fitting parameters for the **2,6-OMe** device also indicate a nominal dominance of the de-trapping process during de-excitation, its overall retention remains the lowest (~21%). This apparent discrepancy arises from the minimal charge trapping during the photo-excitation stage, resulting in a significantly reduced population of stored carriers available for delayed release. Consequently, despite the presence of de-trapping dynamics, the limited trap occupancy in **2,6-OMe** leads to a much weaker persistent photocurrent response.

To probe the thermally activated, near-band-edge trap-assisted charge transport mechanism, temperature-dependent current-voltage (I-V) measurements were carried out, as presented in Figure S34-S35, ESI. The thermal activation energy (E_a) was subsequently extracted from the temperature-dependent I-V characteristics using the Arrhenius relation (Eq. 5):

$$\ln(\sigma) = \ln(\sigma_0) - \frac{E_a}{k_B T} \quad (5)$$

Here, σ represents the electrical conductivity, extracted from the slope of the linear region of the I-V characteristics, while k_B and T denote the Boltzmann constant and absolute temperature, respectively. The thermal activation energy (E_a) was determined from the slope of the $\ln(\sigma)$ versus $1/k_B T$ plot. The extracted activation energies for the **2,4-OMe**, **3,5-OMe**, and **2,6-OMe** devices are 86.41 meV, 98.89 meV, and 50.27 meV, respectively. The relatively higher E_a values for the **2,4-OMe** and **3,5-OMe** devices indicate the presence of deeper near-band-edge trap states, whereas the lower activation energy in **2,6-OMe** suggests comparatively shallower traps or reduced trap-assisted transport.

Conclusions

In this work, we report a series of synthetically simple isomeric donor-acceptor-donor (DAD) triads that display excellent synaptic memory response with a two-electrode system under light illumination. The synaptic response can be tuned by simply changing the position of the donor -OMe groups in the DAD molecule and thereby integrating molecular engineering with device performance. The best performing DAD isomer, **2,4-OMe**, successfully emulates a biological synaptic behaviour with a PPF index near 196% when subjected to a 10-second UV light pulse illuminated at an interval of 2 seconds. Other synaptic characteristics, such as EPSC, IPSC, and ENDP, were also demonstrated in this memory device, and within a more general context they establish a novel approach toward organic optoelectronic neuromorphic computing.

Experimental Procedures



Materials: 2,6-dimethoxybenzaldehyde and *p*-xylylene dicyanide were purchased from TCI India. 2,4-dimethoxybenzaldehyde and 3,5-dimethoxybenzaldehyde were purchased from Sigma Aldrich, and were used as received. Merck ACS-grade solvents were used for the syntheses, and spectroscopy grade solvents were used for crystallization and all spectroscopy studies.

¹H NMR and ¹³C NMR: The ¹H NMR and ¹³C NMR spectra were recorded on a Bruker AVANCE 300 spectrometer (400 MHz) using CDCl₃ as the solvent. The shifts (δ) are given in ppm.

HRMS: The high-resolution mass spectra (HRMS) of the compounds were recorded on QTOF Micro YA263 mass spectrometer in electrospray ionization (ESI) mode

UV-Vis and fluorescence spectroscopy: The solution and solid-state UV-Vis absorption spectra were recorded with a Shimadzu UV-2401C spectrophotometer. The solid-state absorption spectra were recorded with sample coated (thin film) quartz plate. All emission spectra were recorded on a HORIBA Jobin Yvon Fluorolomax-4 spectrofluorometer in the solid state using a solid-state sample holder and the data was collected in front face mode.

Fluorescence life-time: Time-resolved emission measurements of solid crystalline powder samples were carried out on a modular time-correlated single photon counting (Horiba) spectrometer equipped with a Delta Flex detector PPD850.

Scanning electron microscopy (SEM): SEM images of the sample were recorded on a ZEOL- JSM-7610F Schottky Field Emission Scanning Electron Microscope. Samples (2 mg per 1 mL DMF solution) were drop-casted on a Silicon wafer and dried at ambient condition to get a film. The film samples were gold-coated prior to SEM experiment. For film thickness study, the film coated glass slide was attached to a vertical sample holder and the images were collected in vertical sample geometry.

FT-IR: The IR spectra of the DAD crystals were recorded in a Parkin Elmer LX-1 FT-IR spectrometer in ATR mode.

Powder X-ray Diffraction (PXRD): PXRD data of the compounds **3,5-OMe**, **2,4-OMe** and **2,6-OMe** were collected on a Bruker D8 Advanced Diffractometer with Cu K α radiation ($\lambda = 1.5418 \text{ \AA}$), operating at 40 kV and 40 mA. The Lynxeye detector was utilized for data acquisition with a scanning rate of 0.2 seconds per step over a 2θ range of 0° to 50°. For checking the crystallinity of the thin films, the sample solution (2mg/mL) were drop-casted on a glass plate kept at 50 °C (on a hotplate) and dried there in open

air for 30 minutes. The dried samples were subjected for analysis. View Article Online
DOI: 10.1039/D6SC01505X

Single-crystal X-ray diffraction analysis: The single-crystal XRD data of all compounds were collected using a Microfocus D8 venture APEX 3 diffractometer (Bruker) equipped with a CCD area detector and by using MoK α radiation ($\lambda = 0.71069 \text{ \AA}$). The SAINT (v. 8.38A) program was used for data reduction, which were then analysed using XPREP (APEX 3, ver. 2017.3-0).⁴⁴ The SADABS program was used for absorption correction.⁴⁵ The structures were solved by SHELXT (version 2018/2)⁴⁶ and refined by using SHELXL-2014 included in the APEX 3 suite.⁴⁷⁻⁵⁰ All non-hydrogen atoms were refined anisotropically, whereas the positions of the hydrogen atoms were calculated and refined isotopically. The crystallographic data for **3,5-OMe**, **2,4-OMe** and **2,6-OMe** have been deposited with the Cambridge Crystallographic Data Centre (CCDC) under deposition nos. 2304045, 2304044 and 2359645, respectively. Pore analysis of the crystals and the preparation of crystallographic graphics/images were carried out in Mercury.⁵¹

Theoretical calculations: All of the theoretical calculations were carried out using the Gaussian 16 program suite.⁵² Density functional theory (DFT) with hybrid B3LYP functionals⁵³⁻⁵⁵ and the 6-31G(d,p) basis sets were used for gas-phase geometry optimization of the compounds by using input coordinates from respective crystal structures. TDDFT calculation were carried with hybrid CAM-B3LYP functional and 6-31G(d,p) basis set.⁵⁶ Tomasi's polarizable continuum model (PCM) was used for describing the solvent effect on the HOMO-LUMO gap of the compound. The output structures were visualized by using the Chemcraft software.⁵⁷

Synthetic Procedure

Synthesis of 2,4-OMe: A 100 mL round-bottom flask was charged with 2,4 dimethoxybenzaldehyde (0.332 g, 2 mmol) and *p*-xylylene dicyanide (0.157 g, 1 mmol) in 30 mL of methanol, along with potassium *t*-butoxide (0.5 g) and 5-6 drops of tetrabutylammonium hydroxide (TBAH) was added additionally to the reaction mixture. The resulting mixture was heated at 70 °C for 4 h. The product mixture was filtered and the crude was dried in air to obtain yellow-coloured solid product of **2,4-OMe** (0.293 g, 65%). Slow evaporation of the crude product from CHCl₃ solution yielded cuboidal-shaped yellow-coloured crystals which were segregated under optical microscope and dried in air. ¹H NMR (400 MHz, CDCl₃, δ in ppm): 8.26 (*d*, *J* = 9.0 Hz, 1H, ArH), 7.98 (s, 1H, HC-N), 7.74 (s, 1H, ArH), 6.63 (q, 4H, ArH), 6.51 (d, 1H, ArH), 3.90 (s, 6H, OCH₃). HRMS calculated for C₂₈H₂₄N₂O₄ is 453.1736, obtained *m/z* = 453.1816. (M +1). Melting point: 216–221 °C.



Synthesis of 2,6-OMe: A 100 mL round-bottom flask was charged with 2,4-dimethoxybenzaldehyde (0.333 g, 2 mmol) and p-xylylene dicyanide (0.157 g, 1 mmol) in 30 mL of methanol, along with potassium t-butoxide (0.5 g) and 5-6 drops of tetrabutylammonium hydroxide (TBAH) was added additionally to the reaction mixture. A catalytic amount of glacial acetic acid was added to this solution, and the resulting mixture was heated at 90 °C for 4 h. The product mixture was filtered and the crude was dried in air. Cuboidal-shaped pale-yellow crystals of **2,6-OMe** were obtained from DMSO after 20 days which was segregated and dried in air (0.316 g, 70%). ¹H NMR (400 MHz, CDCl₃, δ in ppm): 8.26 (d, *J* = 9.0 Hz, 1H, ArH), 7.98 (s, 1H, HC-N), 7.28 (t, 1H, ArH), 6.58 (q, 4H, ArH), 3.85 (s, 6H, OCH₃). HRMS calculated for C₂₈H₂₄N₂O₄ is 453.1736, obtained *m/z* = 453.1814 (*M* + 1). Melting point: 190–196 °C.

Synthesis of 3,5-OMe: A 100 mL round-bottom flask was charged with 3,5-dimethoxybenzaldehyde (0.332 g, 2 mmol) and p-xylylene dicyanide (0.157 g, 1 mmol) in 30 mL of methanol, along with potassium t-butoxide (0.5 g) and 5-6 drops of tetrabutylammonium hydroxide (TBAH) was added additionally to the reaction mixture. A catalytic amount of glacial acetic acid was added to this solution, and the resulting mixture was heated at 90 °C for 4 h. The product mixture was filtered and the crude was dried in air. Cuboidal-shaped bright green crystals of **3,5-OMe** were obtained from DMSO after 15 days which was segregated and dried in air (0.343 g, 76%). ¹H NMR (400 MHz, CDCl₃, δ in ppm): 7.78 (d, *J* = 8 Hz, 2H, ArH), 7.60 (s, 1H, HC-N), 7.11 (t, 1H, ArH), 6.59 (q, 4H, ArH), 3.88 (s, 6H, OCH₃). HRMS calculated for C₂₈H₂₄N₂O₄ is 453.1736, obtained *m/z* = 453.1814 (*M* + 1). Melting point: 190–196 °C.

Crystallization of DAD isomers: Cuboidal shaped yellow-coloured crystals of **2,4-OMe** crystals were obtained by slow evaporation of CHCl₃ solution at room temperature. cuboidal shaped pale-yellow coloured crystals of **2,6-OMe** crystals were obtained from DMSO solution by keeping the solution at room temperature for 20 days. **3,5-OMe** crystals were obtained from DMSO solution keeping at room temperature for 15 days which led to growth of cuboidal shaped bright green-coloured crystals.

Device preparation: The synaptic memory devices were fabricated via simple spin-casting method. The DAD isomer crystals were each dissolved in DMF (2 mg/mL) to prepare the inks for spin-coating. The inks were spin-coated at a speed 1500 rpm for 15 s on a pre-cleaned FTO coated glass keeping a little portion bared by using non-adhesive Teflon tape, followed by drying on a hotplate at 60 °C for 2 minutes. The spin coating and drying process was repeated 10 times. Finally, the devices were completed by painting top and bottom electrodes on the film and the bared portion on the FTO by using highly conducting Ag

paste (Techinstro). The final devices are shown schematically in Figure 1a.

DOI: 10.1039/D6SC01505K

Author contributions

We strongly encourage authors to include author contributions and recommend using [CRediT](#) for standardised contribution descriptions. Please refer to our general author guidelines for more information about authorship.

Conflicts of interest

There are no conflicts to declare.

Data availability

A data availability statement (DAS) is required to be submitted alongside all articles. Please read our full guidance on data availability statements for more details and examples of suitable statements you can use.

Acknowledgements

M. K. P. acknowledges SERB India for start-up research grant (F. No. SRG/2020/000943) and UGC, New Delhi, India for a start-up research grant (No. F.30-530/2020(BSR)). MB thanks SVMCM scholarship, Govt of West Bengal for fellowship. DD thank the Council for Scientific and Industrial Research (CSIR), New Delhi for fellowship. M. K would like to thank UGC, Govt. of India, for providing a research fellowship (NTA ref. No- 211610081286). R. N. G wishes to thank the Science and Engineering Research Board, Govt. of India (File no. – EEQ/2023/000219) for financial support. This project was partially funded by New York University Abu Dhabi (AD073). Additionally, this material is based on works supported by Tamkeen under NYUAD RRC Grant No. CG011.



References

- 1 J. Wang, Y. Lin, J. You, T. Yu, W. Meng and L. Sun, *Adv. Intell. Syst.*, 2025, 2401057.
- 2 Y. Zhang, Z. Ma, Z. Chen, S. Poddar, Y. Zhu, B. Han, C. L. J. Chan, Y. Ding, X. Kong and Z. Fan, *Adv. Intell. Syst.*, 2024, **6**, 2300586.
- 3 R. Shenoy, A. Tudor, D. Nathan, A. Deo, Z. Rong, C. M. Shaffer, C. D. Danesh, B. Suresh and Y. Chen, *Adv. Intell. Syst.*, 2022, **4**, 2200105.
- 4 L. Zhang, H. Yu, C. Xiao, J. Si, H. Xu, W. Zhu and L. Wang, *Adv. Electron. Mater.*, 2021, **7**, 2000945.
- 5 M. K. Hota, M. N. Hedhili, N. Wehbe, M. A. McLachlan and H. N. Alshareef, *Adv. Mater. Interfaces*, 2016, **3**, 1600192.
- 6 E. E. Josberger, Y. Deng, W. Sun, R. Kautza and M. Rolandi, *Adv. Mater.*, 2014, **26**, 4986–4990.
- 7 D. Sarkar, J. Tao, W. Wang, Q. Lin, M. Yeung, C. Ren and R. Kapadia, *ACS Nano*, 2018, **12**, 1656–1663.
- 8 J. Yang, H. Cho, R. Ryu, M. Ismail, C. Mahata and S. Kim, *ACS Appl. Mater. Interfaces*, 2021, **13**, 33244–33252.
- 9 T. Zhang, C. Fan, L. Hu, F. Zhuge, X. Pan and Z. Ye, *ACS Nano* 2024, **18**, 16236–16247.
- 10 S. L. Gao, L. P. Qiu, J. Zhang, W. P. Han, S. Ramakrishna and Y. Z. Long, *ACS Appl. Electron. Mater.* 2024, **6**, 1542–1561.
- 11 V. M. Poole, S. J. Jokela and M. D. McCluskey, *Sci. Rep.* 2017, **7**, 6659.
- 12 Z. Xiao and J. Huang, *Adv. Electron. Mater.*, 2016, **2**, 1600100.
- 13 M. Loizos, K. Chatzimanolis, K. Anagnostou, K. Rogdakis and E. Kymakis, *ACS Appl. Electron. Mater.*, 2025, **8**, 3610.
- 14 B. Pillai, P. De Souza and M. Merlyne, *ACS Appl. Mater. Interfaces*, 2017, **9**, 1609–1617.
- 15 M. Farronato, P. Mannonci, M. Melegari, S. Ricci, C. M. Compagnoni, D. Ielmini, *Adv. Mater.* 2023, **35**, 2205381.
- 16 Y.-C. Chiang, C.-C. Hung, Y.-C. Lin, Y.-C. Chiu, T. Isono, T. Satoh, W.-C. Chen, *Adv. Mater.* 2020, **32**, 2002638.
- 17 T.-W. Chang, Y.-S. Li, N. Matsuhisa, C.-C. Shih, *J. Mater. Chem. C* 2022, **10**, 13372.
- 18 C. Zheng, C. Li, H. S.-T. Yuan and Y. Zhou, *Adv. Electron. Mater.*, 2020, **6**, 2000641.
- 19 H. Roh, H. Yue, H. Shuwen, C. K. Hang, H. Kulik and A. Gumyusenge, *Adv. Funct. Mater.*, 2023, **33**, 2304893.
- 20 L. Wang, C. Zheng, J. Fu, J. Hua, J. Chen, J. Gao, H. Ling, L. Xie and W. Huang, *Adv. Electron. Mater.*, 2022, **8**, 2200155.
- 21 H. Guo, J. Guo, Y. Wang, H. Wang, S. Cheng, Z. Wang, Q. Miao and X. Xu, *ACS Appl. Mater. Interfaces*, 2024, **16**, 66948–66960.
- 22 J. Zhang, D. Liu, S. Shi, Q. Yang, B. Yang, P. Guo, L. Fang, S. Dai, L. Xiong and J. Huang, *npj Flex. Electron.*, 2022, **6**, 30.
- 23 M. M. H. Tanim, Z. Templin and F. Zhao, *Micromachines* 2023, **14**, 235.
- 24 Z. Feng, M. Comi, Y. Ren, D. Sredojevic, S. Attar, J. Yang, Z. Wang, R. Chen, S. Han, M. Al-Hashimi and Y. Zhou, *ACS Mater. Chem. C*, 2022, **10**, 16604.
- 25 K. Chen, H. Hu, H. B. Gobeze, W. J. Lee, A. Abtahi, K. S. Schanze and J. Mei, *Nat. Photonics*, 2023, **17**, 629–637.
- 26 Y. Lee and T. W. Lee, *Acc. Chem. Res.*, 2019, **52**, 964–974.
- 27 S. Liu, J. Zeng, Z. Wu, H. Hu, A. Xu, H. Huang, W. Chen, Z. Yu, Y. Zhao, R. Wang, T. Han, C. Li, P. Gao, H. Kim, S. J. Baik, R. Zhang, Z. Zhang, P. Zhou and G. Liu, *Nat. Commun.*, 2023, **14**, 7655.
- 28 T. F. Yu, H. Y. Chen, M. Y. Liao, H. C. Tien, T. T. Chang, C. C. Chueh and W. Y. Lee, *ACS Appl. Mater. Interfaces*, 2020, **12**, 33968–33978.
- 29 R. Jia, X. Wu, W. Deng, X. Zhang, L. Huang, K. Niu, L. Chi and J. Jie, *Adv. Funct. Mater.*, 2019, **29**, 1905657.
- 30 Y. Chen, H. Wang, Y. Yao, Y. Wang, C. Ma and P. Samori, *Adv. Mater.*, 2021, **33**, 2103369.
- 31 H. Chen, Y. Cai, Y. Han and H. Huang, *Angew. Chem. Int. Ed.*, 2024, **63**, e202313634.
- 32 C. Eckel, J. Lenz, A. Melianas, A. Salleo and R. T. Weitz, *Nano Lett.*, 2022, **22**, 973–979.
- 33 M. Kangsabanik, R. Sarkar, J. Chowdhury and R. N. Gayen, *J. Alloys Compd.*, 2025, **1010**, 177758.
- 34 S. Feng, J. Li, L. Feng, Z. Liu, J. Wang, C. Cui, O. Zhou, L. Deng, H. Xu, B. Leng, X. Q. Chen, X. Jiang, B. Liu and X. Zhang, *Adv. Mater.*, 2023, **35**, 2308090.
- 35 P. Rajabi Kalvani, A. Parisini, M. Pavesi, et al. *Adv. Electron. Mater.* 2025, **11**, e00072.
- 36 J. Kim, E. C. Park, W. Shin, R-H Koo, C-H Han, H Y. Kang, T G Yang, Y Goh, K. Lee, D. Ha, S. S. Cheema, J. K. Jeong, D. Kwon, *Nature Commun*, 2024, **15**, 9147.
- 37 D. Cai, J. Wang, T. Zhao, M. Shen, Y. Liu, T. Zhang, F. Zhang, Y. Wang, Y. Jiang, D. Gu, *Adv. Sci*, 2026, **13**, e11168.
- 38 Y. Li, J. Lu, D. Shang, Q. Liu, S. Wu, Z. Wu, X. Zhang, J. Yang, Z. Wang, H. Lv, M. Liu, *Adv Mater*, 2020, **32**, 2003018.
- 39 SYJ H. Zhou, L. Cong, J. Ma, B. Li, M. Chen, H. Xu, Y. Liu, *J. Mater. Chem. C*, 2019, **7**, 13149.
- 40 K. Liu, M. Sakurai, M. Aono, D. Shen, *Adv. Funct. Mater.* 2015, **25**, 3157.
- 41 V. M. Kalygina, A. V. Tsymbalov, A. Almaev, B. O. Kushnarev, V. L. Oleinik, J. V. Petrova, P. A. Yunin, *IEEE Sens. J.* 2023, **23**, 15530.
- 42 S. Nandi, S. Ghosal, M. Meyyappan and P. K. Giri, *Mater. Horiz.*, 2025, **12**, 4274–4288.
- 43 Z. Ren, S. Wang, B. Meng, H. Liu, Q. An, L. Su, R. Chen, *ACS Appl. Mater. Interfaces* 2026, **18**, 6191–6199.
- 44 Bruker AXS Inc., APEX3, Version 2017.3-0; SAINT, Version 8.38A, Bruker AXS Inc., Madison, WI, 2012, <https://www.bruker.com>.
- 45 G. M. Sheldrick, SADABS, University of Göttingen, Göttingen, Germany, 1996; part of Bruker APEX3 software package (Version 2017.3-0), Bruker AXS, Madison, WI, 2017.
- 46 G. M. Sheldrick, SHELXTL XT – Crystal Structure Solution, Version 2014/4, Bruker AXS, Madison, WI, 2014.



ARTICLE

Journal Name

- 47 G. M. Sheldrick, SHELXL-2014, University of Göttingen, Göttingen, Germany, 2014.
- 48 G. M. Sheldrick, *Acta Crystallogr., Sect. A*, 2015, **71**, 3–8.
- 49 G. M. Sheldrick, *Acta Crystallogr., Sect. A*, 2008, **64**, 112–122.
- 50 H. Liu, *Acta Crystallogr., Sect. E*, 2010, **66**, o1582.
- 51 C. F. Macrae, I. Sovago, S. J. Cottrell, P. T. A. Galek, P. McCabe, E. Pidcock, M. Platings, G. P. Shields, J. S. Stevens, M. Towler and P. A. Wood, *J. Appl. Crystallogr.*, 2020, **53**, 226–235.
- 52 M. J. Frisch et al., Gaussian 16, Revision A.03, Gaussian, Inc., Wallingford, CT, 2016
- 53 A. D. Becke, *Phys. Rev. A*, 1988, **38**, 3098–3100.
- 54 C. Lee, W. Yang and R. G. Parr, *Phys. Rev. B*, 1988, **37**, 785–789.
- 55 M. Cossi, V. Barone, R. Cammi and J. Tomasi, *Chem. Phys. Lett.*, 1996, 255, 327–335.
- 56 T. Yanai, D. P. Tew and N. C. Handy, *J. Chem. Phys.*, 2004, **124**, 104106.
- 57 Chemcraft, Version 1.8 (Build 682), <https://www.chemcraftprog.com>.

View Article Online
DOI: 10.1039/D6SC01505K

Open Access Article. Published on 14 May 2026. Downloaded on 5/16/2026 12:32:10 PM.
This article is licensed under a Creative Commons Attribution-NonCommercial 3.0 Unported Licence.



Chemical Science Accepted Manuscript

The crystallographic data for 3,5-OMe, 2,4-OMe and 2,6-OMe have been deposited with the Cambridge Crystallographic Data Centre (CCDC) under deposition nos. 2304045, 2304044 and 2359645, respectively. All other data are available from the authors upon reasonable request.

